Proceedings of the 4th International Conference on Mathematical Physics and Computational Simulation
DOI: 10.54254/2753-8818/2026.34127

Design and Electromagnetic Mechanism Investigation of a Tin Triangular Wedge Metasurface Broadband Absorber in the Visible Spectrum

Yishuo Feng

School of Physics and Optoelectronics, South China University of Technology, Guangzhou, China
17839863359@163.com

Abstract. This paper proposes a triangular wedge metasurface absorber. It uses a metal-dielectric-metal stack. The top layer is a triangular wedge array. A dielectric spacer sits in the middle. The bottom is a metal reflective layer.We simulate the device with the finite element method. It shows strong broadband absorption. Average absorption exceeds 93% from 300 to 800 nm. Peaks reach nearly 99% at several wavelengths.Field maps reveal why absorption is so high. Surface plasmon resonance, localized plasmon resonance, and Fabry-Pérot cavity resonance all play a part. They work together to trap light.The design still works well with small geometric errors. That makes fabrication easier.This work can guide the design of photodetectors, solar cells, and UV optoelectronic devices.

Keywords: Metasurface, Visible light, TiN

1. Introduction

Global energy demand keeps rising and the environment suffers. Renewable energy is now widely seen as a sustainable solution. Solar energy stands out. It is abundant and available everywhere. We mainly harness it through two routes. Photothermal conversion is one. Photovoltaic conversion is the other. Both require effective light harvesting across the solar spectrum. Most solar energy falls in the visible and near-ultraviolet range. Broadband absorbers with high efficiency and stable performance are therefore in great demand. Yet they remain a key challenge for practical solar devices [1].Metamaterials are built from subwavelength structures. They manipulate electromagnetic waves beyond the reach of natural materials. Metasurfaces are essentially flat metamaterials. They are ultra-thin, low-loss, and easy to integrate. Such traits make them ideal for high-performance absorbers. By adjusting the geometry, size, and layout of these tiny structures, metasurface absorbers capture waves efficiently and shape the spectrum as needed [2, 3].

Metasurface absorbers have been studied extensively worldwide. Foreign groups have proposed metallic cavity arrays and multilayer stacks [4]. Domestic teams have designed hollow arrays, grid composites and multilayer disks [5]. Broadband absorption and polarization insensitivity have both advanced greatly. Still, complex structures and fabrication difficulty remain major hurdles.

This study focuses on a triangular wedge metasurface absorber. It targets efficient light harvesting in the visible and near-ultraviolet range.The device has three layers from top to bottom. A triangular

© 2026 The Authors. This is an open access article distributed under the terms of the Creative Commons Attribution License 4.0 (https://creativecommons.org/licenses/by/4.0/).

DOI: 10.54254/2753-8818/2026.34127

wedge resonator array sits on top. A dielectric spacer lies in the middle. A metal reflective substrate forms the bottom. Together they create a metal-dielectric-metal stack.Most existing absorbers use disks or cylinders. The triangular wedge differs from these [6]. It supports a wider range of coupling modes. Multiple resonant cavities are built into the design. These features improve broadband impedance matching.We use the finite element method to study its absorption spectrum. At resonant wavelengths, high absorption occurs. We analyze the electric field and thermal loss maps to understand why. The physics behind this strong absorption becomes clear from these distributions. Fabrication always involves some geometric error. We test how such tolerances affect absorption. The results confirm that the design is feasible in practice.These findings can guide the design of practical devices. Examples include photodetectors, solar cells and optical filters for visible and ultraviolet operation [7].

2. Structural description and modeling

2.1. Material selection and structural description

This work designs a metasurface absorber. It uses a simple metal-dielectric-metal stack. Three layers sit from top to bottom. The top is a titanium nitride triangular wedge array. A silicon dioxide spacer sits in the middle. The bottom is a continuous titanium nitride reflective layer. Fig. 1(b) shows the structure.The top layer captures incoming light. It is built from three rectangular nanobars. Each bar sits 120 degrees apart from the others. Together they create a trefoil pattern on the plane.Silicon dioxide fills the middle layer. It guides the waves and forms a cavity. The material itself introduces little loss.The bottom TiN layer stops light from passing through. It also acts as the back reflector for the Fabry-Pérot cavity.

Fig. 1(b) sketches the unit cell. The bottom TiN thickness is labeled h_1. Incident light gets fully reflected by this layer. Transmittance is nearly eliminated.The SiO_2 spacer thickness is denoted h_2. It supplies the necessary phase matching. Both surface plasmon resonance and guided-mode resonance are supported here.The wedge height is h_3. Its tip width is w. Fig. 1(c) gives the top view. The inclination angle θ sets the graded effective refractive index.

Through iterative numerical simulation optimization, the finalized core structural parameters are as follows: period $P = 400nm$, TiN reflective substrate thickness $h_1 = 400nm$, SiO_2 layer thickness $h_2 = 100\,nm$, triangular wedge height $h_3 = 400\,nm$, top width $w = 30nm$,wedge inclination angle $\theta = 120^\circ$

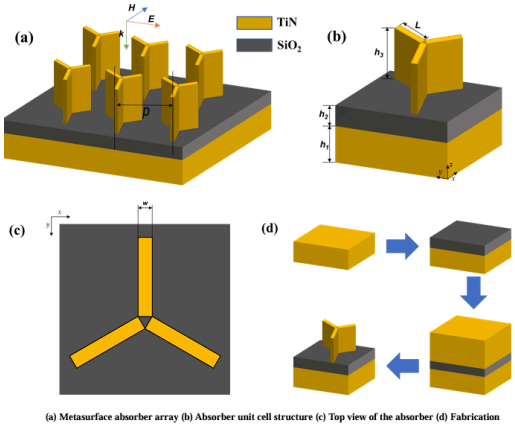


Figure 1. Schematic diagram of the metasurface and fabrication process flow

DOI: 10.54254/2753-8818/2026.34127

TiN is chosen for the top resonators. It belongs to the refractory metal nitride family [8, 9]. The melting point reaches nearly 2950 degrees Celsius. It also offers good chemical stability and tunable optical properties.The plasmonic resonance of TiN covers visible to near-infrared wavelengths. Noble metals like gold and silver are commonly used in similar roles. However, TiN costs significantly less and withstands much higher temperatures.SiO_2 fills the middle layer. Its refractive index is about 1.45. The material remains stable under heat. It also meets the mechanical requirements well.The optical constants of SiO_2 stay fixed. This allows precise control of field propagation. The parameters align naturally with TiN. Broadband impedance tuning is achieved in this manner.Most conventional absorbers use cylinders or tubes. Our design adopts a triangular wedge instead. Three arms are arranged in rotational symmetry. This layout keeps the device polarization-insensitive. The graded wedge cross-section triggers multiple scattering. It also creates slow-wave effects. Modal coupling is greatly expanded. Strong broadband absorption is realized across the visible to near-ultraviolet range.

2.2. Fabrication process

Fig. 1(d) shows how the device is made.First, we clean the TiN substrate. Acetone and deionized water remove oil and organic residues through ultrasonic agitation. Nitrogen blow-drying follows. A vacuum bake then flattens the surface. This step prepares the substrate for film growth.Next, we deposit a SiO_2 layer by radio-frequency magnetron sputtering. This layer transmits electromagnetic waves. It also isolates the top and bottom TiN layers electrically.Then we sputter a thin TiN film onto the SiO_2 surface. Direct-current magnetron sputtering is used. This TiN layer will support the resonators.We now spin-coat positive photoresist onto the SiO_2 surface. Soft baking hardens the resist. Electron-beam lithography writes the wedge array pattern. Development and fixation yield the resist mask.Thick TiN is deposited under the same conditions used for the reflective layer. The metal fills the mask openings.The sample goes into acetone. The photoresist mask dissolves away. A periodic triangular wedge array remains.In the final step, annealing takes place. We heat the device in a furnace under inert gas. Internal stress eases. The bond between layers grows stronger. Stability improves. Fabrication is now complete.

2.3. Simulation method and boundary conditions

COMSOL is used to simulate the absorption spectrum. The finite element method handles the subwavelength geometry. Reflectance and absorptance are computed directly. This approach suits multilayer stacks and periodic arrays well.A plane wave is launched along the z-axis. It strikes the absorber at normal incidence. The wavelength range spans 300 to 1000 nm.Periodic boundaries are set in x and y. They mimic an infinite array. A perfectly matched layer is added in the z direction. It absorbs outgoing waves and removes artificial reflections. For oblique incidence, Bloch boundaries replace the standard periodic ones.Absorptance is defined as one minus reflectance minus transmittance:

$$A(\lambda) = 1 - R(\lambda) - T(\lambda) \tag{1}$$

where $R(\lambda)$ and $T(\lambda)$ denote the reflectance and transmittance of the absorber. The bottom TiN layer is much thicker than the skin depth. No light passes through. Transmittance is essentially zero. Absorptance then becomes one minus reflectance:

DOI: 10.54254/2753-8818/2026.34127

$$A(\lambda) = 1 - R(\lambda) \tag{2}$$

We only need to measure reflectance. A monitoring plane is placed above the wedge array. It records the reflected intensity.

3. Results and discussion

3.1. Absorption spectral analysis

Fig. 2 gives the absorption spectrum from 300 to 1000 nm. The average absorptance is roughly 94%. Distinct peaks emerge at 330 nm, 437 nm, and 662 nm. These maxima reach 98.52%, 97.27%, and 98.41% respectively. The absorber performs well across this broad range.In contrast to single-mode resonance schemes and the fabrication complexity of multilayer stacking,the triangular wedge achieves a "multi-scale-like" broadband coupling through the graded optical response of a single three-dimensional morphology,the 120° rotationally symmetric design of the triangular wedge ensures polarization-insensitive characteristics, while the three-arm structure provides multiple scattering centers, substantially expanding the resonant modal density.In the visible-ultraviolet band, a three-layer minimalist structure achieves absorption efficiency approaching that of complex stacked designs.

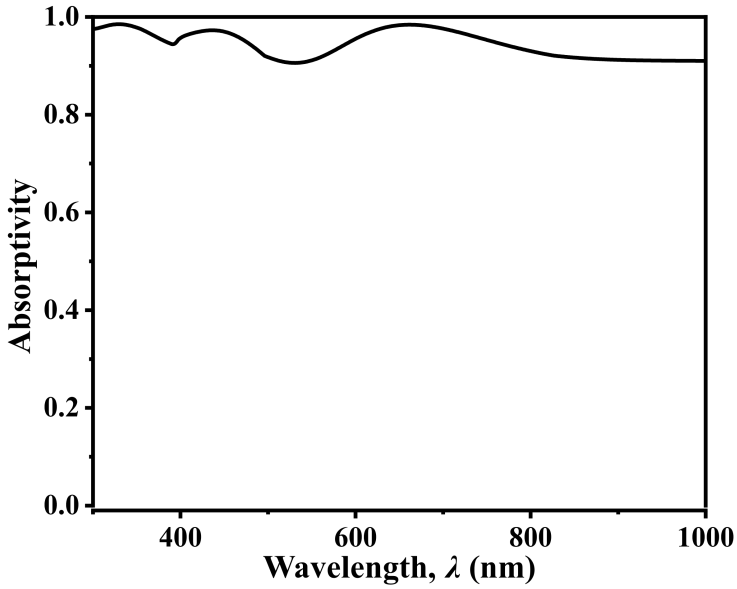


Figure 2. Average absorptance of the metasurface

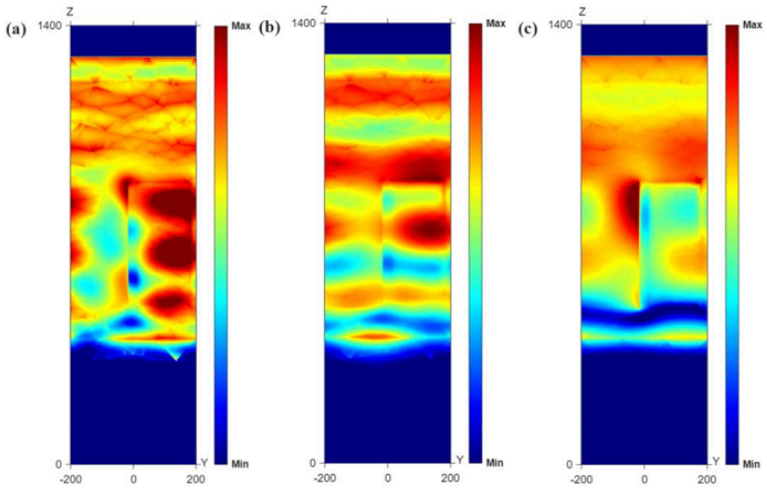
3.2. Absorption mechanism analysis

In conjunction with the magnetic field distribution maps (Fig. 3(a)–(c)), the absorption mechanisms at each characteristic absorption peak are elucidated as follows [10]: Under short-wavelength excitation at 330 nm, the interior of the TiN wedge arms exhibits a distinct multi-node standing-wave magnetic field distribution. This physical image indicates that TiN exhibits strong metallic character in this spectral band, with the real part of its permittivity being a negative value of large magnitude and a significant longitudinal wave vector component of the surface plasmon wave. The incident electromagnetic energy is effectively confined within the metallic structure, with surface currents oscillating back and forth along the arm sidewalls and forming coherent superposition

DOI: 10.54254/2753-8818/2026.34127

between the top and bottom reflection surfaces, establishing a high-order metallic cavity resonance mode. The strong current density at standing-wave nodes is directly converted into Joule heating, rendering the absorption in this band predominantly attributable to ohmic losses within the metallic cavity volume.

At 437 nm, the standing-wave nodes inside the TiN arms drop to two. The spacing between nodes widens. Field intensity at the nodes weakens. The strong magnetic field nonetheless stays within the metallic arms.This change shows the cavity mode shifting from high order to low order. The real part of TiN permittivity decreases. The longitudinal wave vector shrinks. Fewer half-wave interferences fit inside the same height.The strong-field region also moves toward the upper and middle sections of the arms. The confinement center shifts upward accordingly.At this wavelength, the slow-wave effect of the graded wedge starts to appear [11]. The curvature and width vary continuously along the sidewalls. This extends the effective path for surface currents. Group velocity drops. The loss from cavity mode weakening is thereby compensated.At 662 nm, the standing-wave pattern inside the arms almost disappears. The magnetic field clings tightly to the TiN surface. Penetration depth shrinks to the nanometer scale.TiN now approaches a near-zero permittivity state. Localized surface plasmon resonance at the tips reaches its peak [12]. Maximum curvature occurs at the tips. A subwavelength energy dissipation center forms there.Long-wavelength photons can no longer enter deeply into the metal. Energy transport and dissipation occur entirely through surface plasmon polaritons at the metal-dielectric interface.The three cross-sectional field maps illustrate how the mechanism evolves as wavelength increases. Short-wave absorption relies on standing-wave absorption inside the metallic cavity and pre-excitation of tip resonance. Mid-wave absorption builds surface-interface coupling through propagating surface plasmon resonance and guided-mode resonance. Long-wave absorption depends on extreme surface-localized dissipation.The graded wedge cross-section modulates the effective refractive index continuously along the arms [13]. This allows the three mechanisms to reach optimal conditions at different heights. Spatial separation and spectral complementarity are achieved. Broadband synergistic absorption results [14].



(a) 330 nm (b) 437 nm (c) 662 nm

Figure 3. Side-view magnetic field distribution maps [H/H_0]

DOI: 10.54254/2753-8818/2026.34127

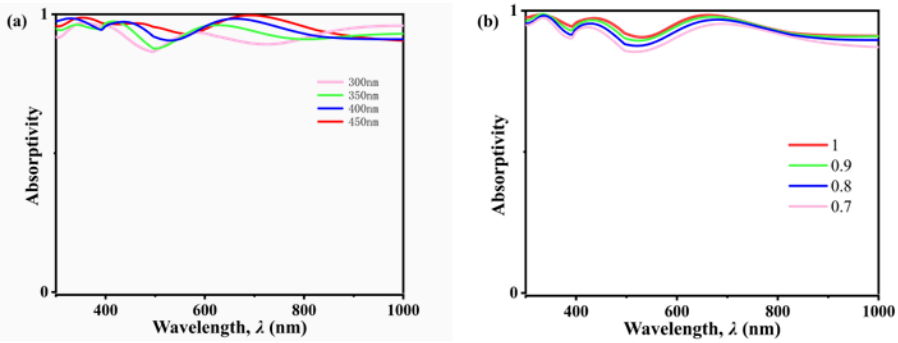
3.3. Influence of geometric parameters on absorptance

The absorption spectrum depends on the geometry [15]. Here we change one variable at a time. We study how etching height and overall scaling affect absorption. This also tells us how easy the structure is to fabricate.

Fig. 4(a) shows absorption spectra for different h_3 heights.At 300 nm, a sharp dip appears between 450 and 550 nm. Absorption here is much lower than at other heights. The structure is simply too short. It cannot support the half-wave resonance of the Fabry-Pérot cavity in this band. So more light reflects away.Yet at wavelengths above 800 nm, this same height absorbs surprisingly well. The short cavity happens to resonate with the long-wave modes.When h_3 rises to 350 nm and 400 nm, the dip gradually disappears. The curve flattens out. Absorption stays above 90% across the entire 300–800 nm range. At these heights, the cavity modes and surface plasmon resonance match well.When $h_3 = 450\,nm$, the short-wavelength end (<400 nm) exhibits relatively enhanced absorptance while the long-wavelength end remains stable, but slight fluctuations appear near 600 nm, suggesting that excessively tall structures may introduce competition from higher-order transverse modes.

Fig. 4(b) illustrates the modulation patterns of the overall scaling factor s on the absorption spectrum. The reference dimensions $(s = 1)$ exhibit the optimal dual-resonant-peak structure, achieving near-perfect absorption peaks at 350 nm and 650 nm (peak value ~99%), with the absorption valley between the two peaks maintained above 95%, and the long-wavelength end (>800 nm) also preserving efficiency above 90%, demonstrating strong synergistic coupling between Fabry-Pérot cavity modes and localized surface plasmon resonance. As s decreases, the dual-resonant-peak structure is preserved but the quality systematically degrades: $s = 0.9$, the peak height slightly decreases, with the valley value dropping to approximately 94%;s= 0.8, the short-wave peak amplitude decreases to approximately 96%, the mid-wave valley (450–500 nm) deepens to approximately 88%, reflecting the blue shift of surface plasmon resonance frequency and deviation from impedance matching conditions caused by the reduction in effective dimensions of the subwavelength structure; $s = 0.7$, the peak height further decreases to approximately 93%, the valley depth drops below 85%, and the long-wavelength end (>800 nm) continuously declines to below 87%, revealing a significant deterioration in modal coupling efficiency. This observation indicates that within the constraint interval $0.9 \leq s \leq 1.0$, the dual-resonance mechanism can effectively maintain broadband performance with average absorptance >90%, providing approximately 10% dimensional tolerance margin for micro-nanofabrication processes such as electron-beam lithography; whereas when $s < 0.9$, plasmon resonance peak shift and enhanced radiation losses cause significant increase in absorption curve fluctuations, necessitating more stringent fabrication precision control. It is worth noting that within the scaling range of 0.9–1.0, the shape of the absorption curve remains highly stable, and the absorption intensity only undergoes a slight redistribution among the various bands, indicating that this design has a moderate tolerance for overall size deviations, which is beneficial for the uniformity control in large-scale manufacturing.

DOI: 10.54254/2753-8818/2026.34127



(a) Etching height sweep (b) Isometric scaling sweep

Figure 4. Parametric sweep results

4. Conclusion

Three effects drive this performance. Sharp tips create localized surface plasmon resonance. Plasmons propagate between the arms and couple with guided-mode resonance. The graded wedge also produces a slow-wave effect.The design uses just a single continuous layer. It avoids complex multilayer stacking or intricate patterns. That makes it easier to fabricate while keeping high performance.Potential uses include photothermal conversion, visible-light detection, and UV photocatalysis. Future work may focus on wedge angle tuning, integration with 2D materials, or adding dynamic control.

References

[1] Nagarajan, L., Gomathy, V., Natraj, N. A. and Arun Kumar, U. (2025). Broadband metasurface absorber achieving ultraviolet-to-mid-infrared efficiency for industrial solar thermal energy conversion. Journal of Materials Science: Materials in Electronics, 36, 2224. https: //doi.org/10.1007/s10854-025-16277-7

[2] Ali, R., Su, W., Ali, M. and Khan, N. M. (2025). Design and optimization of MXene based solar absorber for ultra-broadband solar energy absorption. Diamond and Related Materials, 152, 111986. https: //doi.org/10.1016/j.diamond.2025.111986

[3] Hu, J., Xu, K., Huang, P., Wang, M., Xu, S. and Wei, Q. H. (2024). Hierarchical conical metasurfaces as ultra-broadband perfect absorbers from visible to far-infrared regime. Advanced Functional Materials, 34, 2309229. https: //doi.org/10.1002/adfm.202309229

[4] Patel, S. K., Surve, J., Parmar, J., Katkar, V., Jadeja, R., Taya, S. A. and Ahmed, K. (2022). Graphene-based metasurface solar absorber design for the visible and near-infrared region with behavior prediction using polynomial regression. Optik, 262, 169298. https: //doi.org/10.1016/j.ijleo.2022.169298

[5] Jiang, Y., Deng, J., Lu, Y., Xie, Z. and Chen, Y. (2025). Large-area, flexible, and double-sided metasurface absorber in the visible to near-infrared spectrum. Surfaces and Interfaces, 56, 105708. https: //doi.org/10.1016/j.surfin.2024.105708

[6] Wang, Y., Chen, K., Lin, Y. S. and Yang, B. R. (2022). Plasmonic metasurface with quadrilateral truncated cones for visible perfect absorber. Physica E: Low-dimensional Systems and Nanostructures, 139, 115140. https: //doi.org/10.1016/j.physe.2022.115140

[7] Zeng, P., Zhou, Y., Zhang, C., Yao, J., Pan, M., Fu, Y., Chen, H., Chen, G., Zhao, Q., Guan, X. and Zheng, M. (2024). Nanostructures/TiN layer/Al2O3 layer/TiN substrate configuration-based high-performance refractory metasurface solar absorber. Scientific Reports, 14, 25827. https: //doi.org/10.1038/s41598-024-76118-1

[8] Haque, M. A., Mohsin, A. S. M., Bhuian, M. B. H. and Rahman, M. M. (2024). Analysis of an ultra-broadband TiN-based metasurface absorber for solar thermophotovoltaic cell in the visible to near infrared region. Solar Energy, 284, 113064. https: //doi.org/10.1016/j.solener.2024.113064

[9] Mondal, P., Alkhazragi, O. and Bagci, H. (2025). Enhanced absorption in thin-film silicon solar cells using a broadband plasmonic nanostructure. Optics Express, 33(14), 29118. https: //doi.org/10.1364/OE.566054

DOI: 10.54254/2753-8818/2026.34127

[10] Shin, E., Bangle, R. E., Wilson, N. C., Nikodemski, S. B., Vella, J. H. and Mikkelsen, M. H. (2025). Metasurface-enhanced thermal photodetector operating at gigahertz frequencies. Advanced Functional Materials, 36, 2420953. https: //doi.org/10.1002/adfm.202420953

[11] Cai, B., Wu, L., Zhu, X., Cheng, Z. and Cheng, Y. (2024). Ultra-broadband and wide-angle plasmonic light absorber based on all-dielectric gallium arsenide (GaAs) metasurface in visible and near-infrared region. Results in Physics, 58, 107509. https: //doi.org/10.1016/j.rinp.2024.107509

[12] Wang, B. X., Qin, X., Duan, G. D., Yang, G., Huang, W. Q. and Huang, Z. (2024). Dielectric-based metamaterials for near-perfect light absorption. Advanced Functional Materials, 34(18), 2402068. https: //doi.org/10.1002/adfm.202402068

[13] Wu, L., Yang, L., Zhu, X., Cai, B. and Cheng, Y. (2024). Ultra-broadband and wide-angle plasmonic absorber based on all-dielectric gallium arsenide pyramid nanostructure for full solar radiation spectrum range. International Journal of Thermal Sciences, 201, 109043. https: //doi.org/10.1016/j.ijthermalsci.2024.109043

[14] Song, S., Chen, Y., Chen, S., Hou, J. and Huang, X. (2024). An ultra-broadband high-performance solar energy perfect absorber from deep ultraviolet to mid-infrared. Materials Today Communications, 39, 108712. https: //doi.org/10.1016/j.mtcomm.2024.108712

[15] Cen, C., Liu, X., Lin, Y., Yi, Z., & Zeng, Q. (2025). Metamaterial absorber with ultra-broadband, ultra-high absorption, polarization independence and high-temperature resistance for solar thermal energy harvesting applications. Optics Communications, 575, 131292. https: //doi.org/10.1016/j.optcom.2024.131292